Civil engineering applications of the Asymptotic Expansion Load Decomposition beam model: an overview

Arthur Lebée, G. Corre, M. Ferradi, K. Sab, X. Cespedes

Continuum Mechanics and Thermodynamics manuscript No.
(will be inserted by the editor)

Civil engineering applications of the Asymptotic Expansion Load Decomposition beam model, an overview

Lebée, A. · Corre, G. · Ferradi, M.K. · Sab, K. · Cespedes, X.

the date of receipt and acceptance should be inserted later

Abstract The Asymptotic Expansion Load Decomposition higher-order beam model is based on the classical two-scale asymptotic expansion in the linear elasticity framework. It was successively extended to eigenstrains and to plasticity in small deformations in different papers. The present paper offers a comprehensive and consistent presentation of our approach applied to civil engineering applications.

Keywords Model reduction; Higher-order beam model; Asymptotic expansion; Plasticity; Structural analysis

1 Introduction

Until very recently, most structural engineering offices were designing structures based either on very simple beam models or on complex finite elements modeling. Thanks to the recent development of cloud-computing, a new business model is emerging: online structural analysis. Indeed, cloud computing gives structural engineers access to more powerful computing platforms. It also reduces maintenance operations for the provider since only one system is maintained instead of adapting the software to multiple platforms (Windows, Unix, multiple versions of them, etc.). This is the path chosen by the start-up *Strains engineering* co-founded by Xavier Cespedes in 2014.

The development of such tools requires interactive and real-time simulation softwares. Hence, an efficient mechanical modeling of structural elements and connections is critical. One of the main project of this start-up is the development of a higher-order beam model capable of capturing in more details the influence of the applied load or the boundary conditions for thin-walled and heterogeneous beams. Indeed, traditional design based on simple beam modeling presents the advantage to be easy to understand and to allow rapid

G. Corre · A. Lebée · K. Sab
Laboratoire Navier (UMR 8205), École des Ponts ParisTech, Université Gustave Eiffel, CNRS, Marne-la-Vallée F-77455, France

A. Lebée
E-mail: arthur.lebee@enpc.fr

G. Corre · M.K. Ferradi · X. Cespedes
Strains Engineering, 20 bis rue Sibuet 75012 Paris, France

verification of the results. However, it is not able to give detailed information about local distribution of stresses. In order to obtain more detailed results, complex finite element modeling is necessary. Though, this requires expensive and black-boxed software and is computationally more demanding.

The present paper summarizes and presents a critical review of the Asymptotic Expansion Load Decomposition beam model developped and implemented for *Strains engineering* and published in several contributions [13, 9, 10]. This model originates from the seminal work of Miara and Trabucho [19] for linear elastic beams and was first directly applied by Ferradi et al [13]. Because structural analysis must also take into account eigenstrains such as thermal load, prestress or weakly coupled swelling phenomena, this new type of loading was treated by Corre et al [9] in a linear elastic framework. Finally, since the total plastic strain may be considered as an eigenstrain, the Asymptotic Expansion Load Decomposition model was extended to elasto-plasticity assuming small perturbations in [10].

The paper is organized in two sections. First, the higher-order beam model is derived in the framework of linear elasticity for a given load distribution and some illustrations are briefly presented. Second, the higher-order beam model is extended to elasto-plasticity assuming small perturbations and is validated against a full 3D computation. Finally, limitations and outlooks of the approach are presented.

2 The linear elastic Asymptotic Expansion Load Decomposition beam model

Most beam models are based on *ad-hoc* assumptions on the 3D fields which motivated the denomination *axiomatic*. They rely on an educated guess on the 3D displacement field in a separated form between the longitudinal coordinate and the transverse coordinates. Then, straightforward application of the minimum of potential energy leads to 1D boundary value problems corresponding to the beam model.

Numerous strategies were devised for building the kinematics of the beam. Remarkably, the extended Saint Venant solution from Iesan [15] and the formal asymptotic expansion method [29] delivers almost the same collection of cross-section displacements. Based on the seminal idea from Vogelius and Babuška [30, 31] which also originated the family of "hierarchical models" for plates and shells [1], Miara and Trabucho [19] made two noticeable observations regarding this beam kinematics. First, the formal asymptotic expansion delivers a free family of kinematic enrichment which is dense in the space of the 3D solution. This means that going sufficiently high in the expansion allows arbitrary refinement of the 3D solution. Second, the truncation of this family ensures that the corresponding beam model is asymptotically consistent except at the boundary. Indeed, for loads which do not generate boundary layers, Miara and Trabucho [19] proved a higher-order convergence result. This means that the kinematic enrichment delivered by the formal asymptotic expansion is optimal in terms of approximation error far from the extremities of the beam.

In the following, the asympotic expansion procedure for deriving the AELD kinematics is recalled for a beam under body loads and its link with classical beam models is highlighted. Then, the higher-order beam model is derived and two applications are presented.

2.1 The kinematic enrichment based on the formal asymptotic expansion

In this section, the formal asymptotic expansion procedure is recalled for a linear elastic beam loaded by an arbitrary body force. It is an opportunity to emphasize its close link with

Saint-Venant solution as well as the extension from Iesan [15]. It appears that a series of 3D displacement fields distributed over the cross-section may be obtained as function of the classical beam generalized displacements as well as the longitudinal distribution of the applied load and its higher gradients. Such a basis of "sections modes" may be derived for any given applied load [13] and was extended to prescribed eigenstrains by Corre et al [9].

2.1.1 The 3D problem

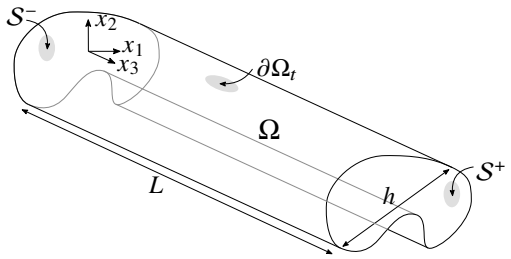

Fig. 1: The beam 3D configuration

We consider a beam occupying the prismatic domain Ω (Figure 1) with a length L and a cross-sectional typical size h. The boundary $\partial\Omega$ is the union of the lateral (free) surface $\partial\Omega_t$ and the two end sections $\mathcal{S}^{\pm}$ (clamped). The longitudinal coordinate is x_3 and the transverse coordinates are x_1 and x_2 denoted as x_α, the corresponding reference frame is denoted $(O, \underline{\boldsymbol{e}}_1, \underline{\boldsymbol{e}}_2, \underline{\boldsymbol{e}}_3)$ where O is an arbitrary point of the plane $x_3 = 0$.

The constitutive material of the beam, relating the stress tensor $\boldsymbol{\sigma}$ to the linearized deformation $\boldsymbol{\varepsilon}$, is only function of the transverse coordinates x_α and invariant in the longitudinal direction. For convenience and without limitation, the corresponding fourth order stiffness tensor $\boldsymbol{C}(x_\alpha)$ is assumed monoclinic with respect to a plane of normal $\underline{\boldsymbol{e}}_3$:

$$C_{\alpha\beta\gamma 3} = C_{333\alpha} = 0. \tag{1}$$

The beam is only subjected to a body load f_i. The corresponding 3D linear boundary value problem writes as:

$$\begin{cases} \underline{\mathbf{div}}\,(\boldsymbol{\sigma}) + \underline{\boldsymbol{f}} = 0 & \text{on } \Omega, \\ \boldsymbol{\sigma} = \boldsymbol{C} : \boldsymbol{\varepsilon}\left(\underline{\boldsymbol{u}}\right) & \text{on } \Omega, \\ \boldsymbol{\sigma} \cdot \underline{\boldsymbol{n}} = 0 & \text{on } \partial\Omega_t, \\ \underline{\boldsymbol{u}} = 0 & \text{on } \mathcal{S}^{\pm}, \end{cases} \tag{2}$$

where $\underline{\boldsymbol{n}}$ is the outer normal to $\partial\Omega_t$, $\underline{\mathbf{div}}$ is the classical divergence operator and $\boldsymbol{\varepsilon}\left(\underline{\boldsymbol{u}}\right)$ is the symmetric part of the displacement gradient.

Scaling and variable separation A new set of coordinates y_i is defined from the global coordinates,

$$(x_1, x_2, x_3) = (hy_1, hy_2, Ly_3)\,, \tag{3}$$

which rewrites the derivation operator as:

$$\nabla_{\underline{\boldsymbol{x}}} = \frac{1}{L}\left(\nabla_{y_3} + \frac{1}{\eta}\nabla_{y_\alpha}\right), \tag{4}$$

as well as the integration over the domain Ω as:

$$\int_\Omega d\Omega = \int_0^L \int_{\mathcal{S}} dx_\alpha dx_3 = L^3\eta^2 \int_0^1 \int_{\mathcal{S}^0} dy_\alpha dy_3 = L^3\eta^2 \int_0^1 \langle\,\rangle\, dy_3, \tag{5}$$

where $\eta = \frac{h}{L}$ is the small parameter related to the slenderness of the beam, $\mathcal{S}^0$ is the scaled cross-section, independent from η and $\langle\,\rangle$ denotes integration on the scaled cross-section.

The body load is assumed to have the following separated form:

$$f_\alpha = \frac{\eta^2}{L}\,\widetilde{f_\alpha}(y_\eta)F(y_3) \quad \text{and} \quad f_3 = \frac{\eta}{L}\,\widetilde{f_3}(y_\eta)F(y_3) \tag{6}$$

where $\widetilde{f_i}$ are cross-section distributions of the load which are modulated by a single longitudinal function $F(x_3)$. In this section, capital letters denote functions of only the y_3 coordinate (except for $\boldsymbol{C}$) and $\widetilde{\bullet}$ denotes functions of only cross-section coordinates y_α.

Expansion The asymptotic expansion method is a formal procedure in which all fields are assumed sufficiently smooth. It yields a cascade of cross-section and longitudinal boundary value problems which are classically solved recursively. In the present case, only the cross-section problems are of interest in order to derive a collection of displacement modes.

The displacement, strain and stress variables are expanded as power series of the small parameter as follows [24, 29, 6]:

$$\underline{\boldsymbol{u}} = L\left(U^0_\alpha(y_3)\underline{\boldsymbol{e}}_\alpha + \eta\underline{\boldsymbol{u}}^1 + \eta^2\underline{\boldsymbol{u}}^2 + \ldots\right), \tag{7}$$

$$\boldsymbol{\varepsilon} = \boldsymbol{\varepsilon}^0 + \eta\boldsymbol{\varepsilon}^1 + \eta^2\boldsymbol{\varepsilon}^2 + \ldots, \tag{8}$$

$$\boldsymbol{\sigma} = \boldsymbol{\sigma}^0 + \eta\boldsymbol{\sigma}^1 + \eta^2\boldsymbol{\sigma}^2 + \ldots \tag{9}$$

and introduced in the rescaled equations of the 3D boundary value problem (2) where each power p of η is identified. In Equation 7, Einstein's implicite summation convention on repeated indices is used. Note that, Greek indices denotes transverse dimensions: $\alpha, \beta\ldots = 1, 2$ and Latin indices denotes all three dimensions: $i, j\ldots = 1, 2, 3$.

The problem being linear, the choice of the starting order has no incidence on the final formulation in terms of physical variable. Here the starting order is chosen so that the leading order of the displacement field is 0. The starting order of the other fields is chosen accordingly and motivates the scaling of the load in Equation (6).

For $p \in \mathbb{N}$, each compatibility equations, boundary conditions and constitutive equations for p and equilibrium equations for $p-1$ yield an auxiliary problem on the cross-section which splits in two uncoupled boundary value problems.

Transverse displacement First, the cross-section displacement problems (transverse mode) $\mathcal{T}^{p+1}$ are gathered for $p \geq 0$:

$$\mathcal{T}^{p+1}: \begin{cases} \sigma^p_{\alpha\beta,\beta} + \sigma^{p-1}_{\alpha 3,3} + \delta_{p3}\widetilde{f_\alpha}F = 0 & \text{on } \mathcal{S}^0, \quad (10a)\\ \sigma^p_{\alpha\beta} = C_{\alpha\beta\gamma\delta}\varepsilon^p_{\delta\gamma} + C_{\alpha\beta 33}\varepsilon^p_{33} & \text{on } \mathcal{S}^0, \quad (10b)\\ \sigma^p_{33} = C_{33\alpha\beta}\varepsilon^p_{\beta\alpha} + C_{3333}\varepsilon^p_{33} & \text{on } \mathcal{S}^0, \quad (10c)\\ \varepsilon^p_{\alpha\beta} = u^{p+1}_{(\alpha,\beta)}, \quad \varepsilon^p_{33} = u^p_{3,3} & \text{on } \mathcal{S}^0, \quad (10d)\\ \sigma^p_{\alpha\beta}n_\beta = 0 & \text{on } \partial\mathcal{S}^0. \quad (10e) \end{cases}$$

where $\boldsymbol{\sigma}^{-1} = 0$ and $\delta_{3p} = 1$ if $p = 3$ and $\delta_{3p} = 0$ else. Transposing the results from [8, 2], for a simply connected cross-section and regular enough $\boldsymbol{C}$ and loadings, this boundary value problem on the displacement u_α^{p+1} is a pure traction (Neumann) problem which is well-posed provided that the applied load is globally self-equilibrating for cross-section translations and rotation:

$$\left\langle \sigma_{\alpha 3,3}^{p-1} + \delta_{p3}\widetilde{f}_\alpha F \right\rangle = 0 \quad \text{and} \quad \left\langle y_\beta \epsilon_{\beta\alpha} \left(\sigma_{\alpha 3,3}^{p-1} + \delta_{p3}\widetilde{f}_\alpha F \right) \right\rangle = 0, \tag{11}$$

where $\epsilon_{\alpha\beta}$ is the permutation operator: $\epsilon_{11} = \epsilon_{22} = 0$, $\epsilon_{12} = +1$, $\epsilon_{21} = -1$. Then, under compatibility conditions (11), the solution is uniquely defined up to the following rigid motion of the section in its plane:

$$u_\alpha^{R,p+1} = U_\alpha^{p+1}(y_3) + y_\beta \epsilon_{\beta\alpha} \Theta^{p+1}(y_3). \tag{12}$$

where U_α^{p+1} is a transverse displacement and Θ^{p+1} a twist rotation.

Longitudinal displacement Second, the longitudinal displacement problems (warping mode) $\mathcal{W}^p$ are obtained for $p \geq 0$:

$$\mathcal{W}^{p+1} : \begin{cases} \sigma_{3\alpha,\alpha}^p + \sigma_{33,3}^{p-1} + \delta_{p2}\widetilde{f}_3 F = 0 & \text{on } \mathcal{S}^0, \quad (13a) \\ \sigma_{\alpha 3}^p = C_{\alpha 3 \beta 3}\, 2\varepsilon_{\beta 3}^p & \text{on } \mathcal{S}^0, \quad (13b) \\ 2\varepsilon_{\alpha 3}^p = u_{3,\alpha}^{p+1} + u_{\alpha,3}^p & \text{on } \mathcal{S}^0, \quad (13c) \\ \sigma_{\alpha 3}^p n_\alpha = 0 & \text{on } \partial\mathcal{S}^0. \quad (13d) \end{cases}$$

Again, for a simply connected cross-section and regular enough $\boldsymbol{C}$ and loadings, this boundary value problem on the displacement u_3^{p+1} is well-posed if the applied load is globally self-equilibrating for the longitudinal translation:

$$\left\langle \sigma_{33,3}^{p-1} + \delta_{p2}\widetilde{f}_3 F \right\rangle = 0. \tag{14}$$

In this case, the solution is uniquely defined up to a uniform longitudinal displacement:

$$u_3^{R,p+1} = U_3^{p+1}(y_3). \tag{15}$$

Resultants and macroscopic equilibrium equations The rigid motion of the section suggests the following definition of the beam resultants at each order $p \geq 0$:

$$N_3^p = \left\langle \sigma_{33}^p \right\rangle, \quad M_\alpha^p = \left\langle y_\alpha \sigma_{33}^p \right\rangle, \quad M_3^p = \left\langle y_\beta \epsilon_{\beta\alpha} \sigma_{\alpha 3}^p \right\rangle \quad \text{and} \quad V_\alpha^p = \left\langle \sigma_{\alpha 3}^p \right\rangle, \tag{16}$$

where N_3^p is the normal traction, M_α^p are the bending moments[1], M_3^p is the moment of torsion and V_α^p are the shear forces.

From the compatibility conditions (10a) and (13a) it is possible to prove that these resultants must comply with the following classical beam equilibrium equations for each $p \geq 0$:

$$\begin{cases} N_{3,3}^p + \delta_{p1} p_3 F = 0, & (17a) \\ M_{\alpha,3}^p - V_\alpha^{p+1} + \delta_{p1}\mu_\alpha F = 0, & (17b) \\ M_{3,3}^p + \delta_{p2}\mu_3 F = 0, & (17c) \\ V_{\alpha,3}^p + \delta_{p2} p_\alpha F = 0. & (17d) \end{cases}$$

[1] It will appear that M_α^p is the working conjugate to the curvature $U_{\alpha,33}^p$ and not the conventional bending moment. Indeed, the classical definition is $m_\alpha^p = \left\langle \epsilon_{\alpha\beta} y_\beta \sigma_{33}^p \right\rangle = \epsilon_{\alpha\beta} M_\beta^p$. This choice is made for convenience.

where $p_\alpha = \left\langle \widetilde{f_\alpha} \right\rangle$ are the transverse loads, $p_3 = \left\langle \widetilde{f_3} \right\rangle$ is the longitudinal load, $\mu_\alpha = \left\langle y_\alpha \widetilde{f_3} \right\rangle$ are distributed bending couples and $\mu_3 = \left\langle y_\beta \epsilon_{\beta\alpha} \widetilde{f_\alpha} \right\rangle$ is a distributed torsion load.

The series of problems are now solved order by order.

2.1.2 First-order problems

Transverse displacement The problem $\mathcal{T}^1$ is not loaded. Consequently, the transverse displacement u^1_α is a rigid motion and the corresponding stress is null:

$$u^1_\alpha = U^1_\alpha(y_3) + y_\beta \epsilon_{\beta\alpha} \Theta^1(y_3) \quad \text{and} \quad \sigma^0_{\alpha\beta} = 0, \quad \sigma^0_{33} = 0. \tag{18}$$

Here, Θ^1 appears as the leading order angle of twist and U^1_α as the second order macroscopic transverse displacement.

Longitudinal displacement The longitudinal displacement problem (warping mode) $\mathcal{W}^1$ writes as:

$$\mathcal{W}^1 : \begin{cases} \sigma^0_{3\alpha,\alpha} = 0 & \text{on } \mathcal{S}^0, \quad (19a) \\ \sigma^0_{\alpha 3} = C_{\alpha 3 \beta 3}\, 2\varepsilon^0_{\beta 3} & \text{on } \mathcal{S}^0, \quad (19b) \\ 2\varepsilon^0_{\alpha 3} = u^1_{3,\alpha} + U^0_{\alpha,3} & \text{on } \mathcal{S}^0, \quad (19c) \\ \sigma^0_{\alpha 3} n_\alpha = 0 & \text{on } \partial\mathcal{S}^0. \quad (19d) \end{cases}$$

The applied load is self-equilibrating and the solution of this boundary value problem writes as:

$$u^1_3 = U^1_3 + y_\alpha U^0_{\alpha,3} \quad \text{and} \quad \sigma^0_{\alpha 3} = 0, \tag{20}$$

where $U^0_{\alpha,3}$ appears as the bending rotation and U^1_3 as the leading order longitudinal displacement.

2.1.3 Second-order problems

Transverse displacement The transverse displacement u^2_α is derived through:

$$\mathcal{T}^2 : \begin{cases} \sigma^1_{\alpha\beta,\beta} = 0 & \text{on } \mathcal{S}^0, \quad (21a) \\ \sigma^1_{\alpha\beta} = C_{\alpha\beta\gamma\delta}\varepsilon^1_{\delta\gamma} + C_{\alpha\beta 33}\varepsilon^1_{33}, & \text{on } \mathcal{S}^0, \quad (21b) \\ \sigma^1_{33} = C_{33\alpha\beta}\varepsilon^1_{\beta\alpha} + C_{3333}\varepsilon^1_{33} & \text{on } \mathcal{S}^0, \quad (21c) \\ \varepsilon^1_{\alpha\beta} = u^2_{(\alpha,\beta)}, \quad \varepsilon^1_{33} = U^1_{3,3} + y_\alpha U^0_{\alpha,33} & \text{on } \mathcal{S}^0, \quad (21d) \\ \sigma^1_{\alpha\beta} n_\beta = 0 & \text{on } \partial\mathcal{S}^0. \quad (21e) \end{cases}$$

Again, the applied load is globally self-equilibrating. The solution of this boundary value problem parametrized by the elongation $U^1_{3,3}$ and the curvatures $U^0_{\alpha,33}$ writes as the linear superposition of each contribution:

$$u^2_\alpha = \widetilde{u}^{e_3}_\alpha\, U^1_{3,3} + \widetilde{u}^{\chi\beta}_\alpha\, U^0_{\beta,33} + U^2_\alpha + y_\beta \epsilon_{\beta\alpha} \Theta^2, \tag{22}$$

where $\widetilde{u}^{e_3}_\alpha$, $\widetilde{u}^{\chi\beta}_\alpha$ are cross-section displacements related to transverse Poisson's effect under pure traction and pure curvatures which are illustrated for a square section in Figure 2. When the section is homogeneous, these correctors have a closed-form expression which is detailed

in [32] for instance. In order to be uniquely defined, the following constraints are applied to all these cross-section displacements:

$$\langle \widetilde{u}_\alpha \rangle = 0 \quad \text{and} \quad \left\langle y_\beta \epsilon_{\beta\alpha} \widetilde{u}_\alpha \right\rangle = 0. \tag{23}$$

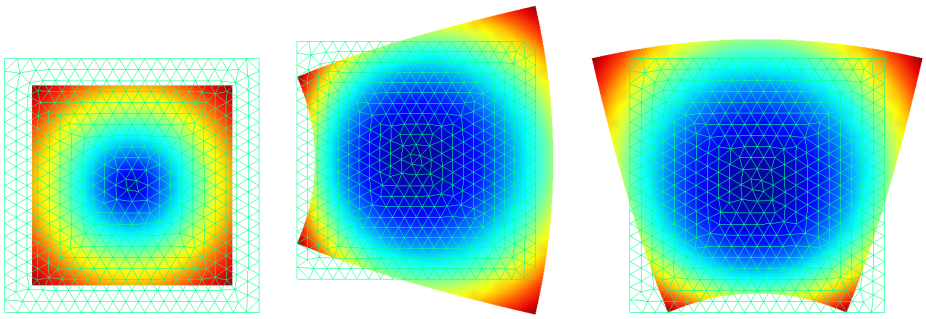

(a) Transverse mode $\widetilde{u}_\alpha^{e_3}$ (b) Transverse mode $\widetilde{u}_\alpha^{\chi_1}$ (c) Transverse mode $\widetilde{u}_\alpha^{\chi_2}$

Fig. 2: Transverse modes related to pure traction and pure curvatures for a homogeneous square section with an isotropic material

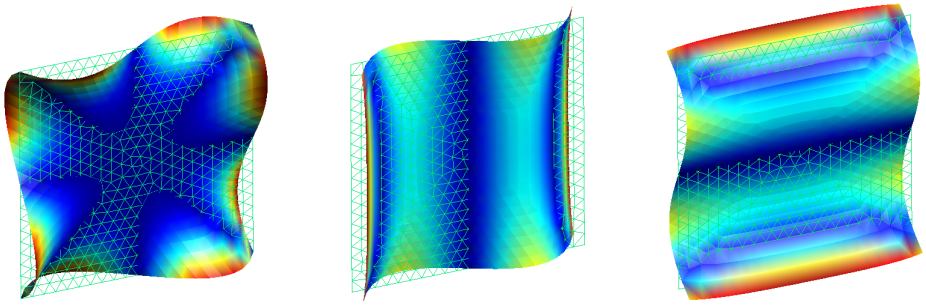

(a) Warping mode $\widetilde{u}_3^{\chi_3}$ (b) Warping mode $\widetilde{u}_3^{V_1}$ (c) Warping mode $\widetilde{u}_3^{V_2}$

Fig. 3: Warping modes related to pure torsion and pure shear forces for a homogeneous square section with an isotropic material

Longitudinal displacement The longitudinal displacement u_3^2 complies with:

$$\mathcal{W}^2 : \begin{cases} \sigma^1_{3\alpha,\alpha} = 0 & \text{on } \mathcal{S}^0, \quad (24a) \\ \sigma^1_{\alpha 3} = C_{\alpha 3 \beta 3}\, 2\varepsilon^1_{\beta 3} & \text{on } \mathcal{S}^0, \quad (24b) \\ 2\varepsilon^1_{\alpha 3} = u^2_{3,\alpha} + y_\beta \epsilon_{\beta\alpha} \Theta^1_{,3} + U^1_{\alpha,3} & \text{on } \mathcal{S}^0, \quad (24c) \\ \sigma^1_{\alpha 3} n_\alpha = 0 & \text{on } \partial\mathcal{S}^0. \quad (24d) \end{cases}$$

The applied load is globally self-equilibrating. The solution of this boundary value problem parametrized by $\Theta^1_{,3}$ and $U^1_{\alpha,3}$ writes as the linear superposition of each contribution:

$$u^2_3 = \widetilde{u}^{\chi_3}_3 \Theta^1_{,3} + U^2_3 + y_\alpha U^1_{\alpha,3}, \tag{25}$$

where $\widetilde{u}^{\chi_3}_3$ is the torsion warping[2] illustrated in Figure 3a. Indeed, the displacement $\widetilde{u}^{\chi_3}_3$ is exactly the solution of the Neumann problem for Saint Venant's torsion. Again, this warping is constrained as follows:

$$\langle \widetilde{u}_3 \rangle = 0. \tag{26}$$

Macroscopic constitutive equations From the solution of second order problems, the first order stress may be written as:

$$\begin{cases} \sigma^1_{\alpha\beta} = \widetilde{\sigma}^{e_3}_{\alpha\beta} U^1_{3,3} + \widetilde{\sigma}^{\chi_1}_{\alpha\beta} U^0_{1,33} + \widetilde{\sigma}^{\chi_2}_{\alpha\beta} U^0_{2,33}, & \text{(27a)} \\ \sigma^1_{\alpha 3} = \widetilde{\sigma}^{\chi_3}_{\alpha 3} \Theta^1_{,3}, & \text{(27b)} \\ \sigma^1_{33} = \widetilde{\sigma}^{e_3}_{33} U^1_{3,3} + \widetilde{\sigma}^{\chi_1}_{33} U^0_{1,33} + \widetilde{\sigma}^{\chi_2}_{33} U^0_{2,33}. & \text{(27c)} \end{cases}$$

Expressing the traction and bending moments leads to the following constitutive equations:

$$\begin{cases} N^1_3 = A_3 U^1_{3,3} + S_1 U^0_{1,33} + S_2 U^0_{2,33}, & \text{(28a)} \\ M^1_1 = S^*_1 U^1_{3,3} + D_1 U^0_{1,33} + D_{12} U^0_{2,33}, & \text{(28b)} \\ M^1_2 = S^*_2 U^1_{3,3} + D^*_{12} U^0_{1,33} + D_2 U^0_{2,33}, & \text{(28c)} \end{cases}$$

where:

$$\begin{cases} A_3 = \left\langle \widetilde{\sigma}^{e_3}_{33} \right\rangle, \quad S_1 = \left\langle \widetilde{\sigma}^{\chi_1}_{33} \right\rangle, \quad S_2 = \left\langle \widetilde{\sigma}^{\chi_2}_{33} \right\rangle, \\ S^*_1 = \left\langle y_1 \widetilde{\sigma}^{e_3}_{33} \right\rangle, D_1 = \left\langle y_1 \widetilde{\sigma}^{\chi_1}_{33} \right\rangle, D_{12} = \left\langle y_1 \widetilde{\sigma}^{\chi_2}_{33} \right\rangle, \\ S^*_2 = \left\langle y_2 \widetilde{\sigma}^{e_3}_{33} \right\rangle, D^*_{12} = \left\langle y_2 \widetilde{\sigma}^{\chi_1}_{33} \right\rangle, D_2 = \left\langle y_2 \widetilde{\sigma}^{\chi_2}_{33} \right\rangle. \end{cases} \tag{29}$$

The modulus A_3 is the traction stiffness, D_1 and D_2 are the bending stiffnesses. It is possible to prove that $S^*_1 = S_1$, $S^*_2 = S_2$ and $D^*_{12} = D_{12}$. The stiffnesses S_1 and S_2 are related to the first moments of inertia. Furthermore, there is a position for O, the origin of the reference frame, such that $S_1 = S_2 = 0$ and rotating the reference frame with respect to $\underline{\boldsymbol{e}}_3$, there is an angle such that $D_{12} = 0$. When the section is homogeneous, this choice of reference frame corresponds to the centroid of the section oriented along one of the principal axis of the second moments of inertia. This is assumed in the following:

$$\begin{cases} N^1_3 = A_3 U^1_{3,3}, & \text{(30a)} \\ M^1_1 = D_1 U^0_{1,33}, & \text{(30b)} \\ M^1_2 = D_2 U^0_{2,33}. & \text{(30c)} \end{cases}$$

Similarly, the torsion is expressed as function of the macroscopic displacements and the eigenstrain:

$$M^1_3 = D_3 \Theta^1_{,3}, \tag{31}$$

where the torsion stiffness is:

$$D_3 = \left\langle y_\gamma \epsilon_{\gamma\alpha} \widetilde{\sigma}^{\chi_3}_{\alpha 3} \right\rangle. \tag{32}$$

Whereas the uncoupling between traction and bending moments may always be satisfied with a proper choice of the reference frame, the uncoupling between torsion is obtained here because of the symmetry assumption (1). This assumption may be released without limiting the approach presented here. Indeed, constitutive equations (30) and (31) would be simply coupled in such a case and would make the derivation more involved.

[2] $\underline{\widetilde{\boldsymbol{u}}}^{\chi_3}_3$ is the warping used by Benscoter [4].

2.1.4 Third-order problems

Transverse displacement The transverse displacement u^3_α is derived through $\mathcal{T}^3$ and loaded by $\Theta^1_{,33}$, $U^2_{3,3}$ and $U^1_{\alpha,33}$. Noticing that the constitutive equation (31) and the torsion equilibrium equation (17c) for $p = 1$, enforce $\Theta^1_{,33} = 0$, it appears that $\mathcal{T}^3$ is exactly the same problem as $\mathcal{T}^2$, incrementing the orders[3].

Longitudinal displacement The longitudinal displacement u^3_3 complies with $\mathcal{W}^3$ and is loaded by $\Theta^2_{,3}$, $U^1_{3,33}$ and $U^0_{\alpha,333}$. The applied load is not globally self-equilibrating for each individual loading. From the constitutive equation (30a) and the equilibrium equation (17a) with $p = 1$ it is deduced that :

$$U^1_{3,33} = -\frac{p_3}{A_3} F. \tag{33}$$

Substituting this in $\mathcal{W}^3$ ensures it is well-posed. Furthermore, it is also convenient to ensure that the load is also self-equilibrating in bending. This is obtained, from the constitutive equations (30b) and (30c) and the equilibrium equation (17b) for $p = 1$:

$$U^0_{1,333} = \frac{V^2_1 - \mu_1 F}{D_1} \quad \text{and} \quad U^0_{2,333} = \frac{V^2_2 - \mu_2 F}{D_2}. \tag{34}$$

Inserting these relations in problem $\mathcal{W}^3$ leads to:

$$\mathcal{W}^3 : \begin{cases} \sigma^2_{3\alpha,\alpha} + \widetilde{\sigma}^{\chi_1}_{33}\frac{V^2_1}{D_1} + \widetilde{\sigma}^{\chi_2}_{33}\frac{V^2_2}{D_2} + \left(\widetilde{f}_3 - \frac{p_3}{A_3}\widetilde{\sigma}^{e_3}_{33} - \frac{\mu_1}{D_1}\widetilde{\sigma}^{\chi_1}_{33} - \frac{\mu_2}{D_2}\widetilde{\sigma}^{\chi_2}_{33}\right) F = 0 & \text{on } \mathcal{S}^0, \quad (35a) \\ \sigma^2_{\alpha 3} = C_{\alpha 3 \beta 3}\, 2\varepsilon^2_{\beta 3} & \text{on } \mathcal{S}^0, \quad (35b) \\ 2\varepsilon^2_{\alpha 3} = u^3_{3,\alpha} + \widetilde{u}^{\chi_1}_\alpha \frac{V^2_1}{D_1} + \widetilde{u}^{\chi_2}_\alpha \frac{V^2_2}{D_2} - \left(\frac{p_3}{A_3}\widetilde{u}^{e_3}_\alpha + \frac{\mu_1}{D_1}\widetilde{u}^{\chi_1}_\alpha + \frac{\mu_2}{D_2}\widetilde{u}^{\chi_2}_\alpha\right) F \\ \qquad + y_\beta \epsilon_{\beta\alpha}\Theta^2_{,3} + U^2_{\alpha,3} & \text{on } \mathcal{S}^0, \quad (35c) \\ \sigma^2_{\alpha 3} n_\alpha = 0 & \text{on } \partial\mathcal{S}^0. \quad (35d) \end{cases}$$

The solution is parametrized by the shear forces V^2_α the applied load F and higher-order beam displacements. It writes as the linear superposition of each contributions:

$$u^3_3 = \widetilde{u}^{V_\alpha}_3 V^2_\alpha + \widetilde{u}^F_3 F + \widetilde{u}^{\chi_3}_3 \Theta^2_{,3} + y_\alpha U^2_{\alpha,3} + U^3_3. \quad \text{with} \quad \langle \widetilde{u}_3 \rangle = 0 \tag{36}$$

The longitudinal displacements $\widetilde{u}^{V_1}_3$ and $\widetilde{u}^{V_2}_3$ are warpings related to shear forces illustrated in Figure (3b) and (3c). Indeed, considering the whole problem $\mathcal{W}^3$ loaded exclusively with shear forces, one can identify the corresponding Neumann problems in Saint Venant's beam theory. Furthermore, the equilibrium equation (35a) considered with only the shear forces loading and integrated on a partial section is actually Jouravskii's Formula [16] which gives a fair estimate of shear stress in thin-walled beams. Finally, $\widetilde{u}^{V_1}_3$ and $\widetilde{u}^{V_2}_3$ are related to the shear lag phenomenon in homogeneous thin-walled beams: when the beam is not enough slender, the longitudinal stress σ_{33} is not exactly the linear distribution derived at leading order (Equation (27c)).

[3] This simplification comes from the symmetry assumption (1) and the scaling chosen for f_α such that bending deflection is of order 0.

Macroscopic constitutive equations From the solution of third order problems, the second-order stress may be written as:

$$\begin{cases} \sigma^2_{\alpha\beta} = \widetilde{\sigma}^{e_3}_{\alpha\beta} U^2_{3,3} + \widetilde{\sigma}^{\chi_1}_{\alpha\beta} U^1_{1,33} + \widetilde{\sigma}^{\chi_2}_{\alpha\beta} U^1_{2,33}, & \text{(37a)} \\ \sigma^2_{\alpha 3} = \widetilde{\sigma}^{V_\beta}_{\alpha 3} V^2_\beta + \widetilde{\sigma}^{F}_{\alpha 3} F + \widetilde{\sigma}^{\chi_3}_{\alpha 3} \Theta^2_{,3}, & \text{(37b)} \\ \sigma^2_{33} = \widetilde{\sigma}^{e_3}_{33} U^2_{3,3} + \widetilde{\sigma}^{\chi_1}_{33} U^1_{1,33} + \widetilde{\sigma}^{\chi_2}_{33} U^1_{2,33} & \text{(37c)} \end{cases}$$

The traction and bending constitutive equations obtained from this stress distribution are identical to equations (30) incrementing the order. The second-order torsion is expressed as function of the macroscopic displacements and the applied load:

$$M^2_3 = D_3 \Theta^2_{,3} + y^S_\alpha \epsilon_{\alpha\beta} V^2_\beta + M^F_3 F, \tag{38}$$

where the torsion induced by the non-uniform distribution of $\widetilde{f_3}$ in the section is $M^F_3 = \left\langle y_\gamma \epsilon_{\gamma\alpha} \widetilde{\sigma}^F_{\alpha 3} \right\rangle$ and the shear center of the beam is defined as:

$$y^S_1 = -\left\langle y_\alpha \epsilon_{\alpha\beta} \widetilde{\sigma}^{V_2}_{\beta 3} \right\rangle \quad \text{and} \quad y^S_2 = \left\langle y_\alpha \epsilon_{\alpha\beta} \widetilde{\sigma}^{V_1}_{\beta 3} \right\rangle. \tag{39}$$

When the section presents two axes of symmetry, the shear center is in O but this is not always true.

2.1.5 Fourth-order and higher-order problems

Transverse displacement The transverse displacement u^4_α is derived through $\mathcal{T}^3$ and loaded by $V^2_\alpha, F, F_{,3}, \Theta^2_{,33}, U^3_{3,3}$ and $U^2_{\alpha,33}$. Taking into account equilibrium equations (17c) and (17d) and constitutive equation (38), the problem may be recast only as function of F and $F_{,3}$, $U^3_{3,3}$ and $U^2_{\alpha,33}$. This substitution ensures also that the compatibility conditions (11) are satisfied. This leads to:

$$\mathcal{T}^4 : \begin{cases} \sigma^3_{\alpha\beta,\beta} + \left(\widetilde{\sigma}^F_{\alpha 3} - \widetilde{\sigma}^{\chi_3}_{\alpha 3} \frac{M^F_3}{D_3} \right) F_{,3} \\ \qquad + \left(\widetilde{f}_\alpha - \widetilde{\sigma}^{V_\beta}_{\alpha 3} p_\beta - \frac{\widetilde{\sigma}^{\chi_3}_{\alpha 3}}{D_3} \left(\mu_3 - y^S_\beta \epsilon_{\beta\gamma} p_\gamma \right) \right) F = 0 & \text{on } \mathcal{S}^0, \quad \text{(40a)} \\ \sigma^3_{\alpha\beta} = C_{\alpha\beta\gamma\delta} \varepsilon^3_{\delta\gamma} + C_{\alpha\beta 33} \varepsilon^3_{33}, \quad \sigma^3_{33} = C_{33\alpha\beta} \varepsilon^3_{\beta\alpha} + C_{3333} \varepsilon^3_{33} & \text{on } \mathcal{S}^0, \quad \text{(40b)} \\ \varepsilon^3_{\alpha\beta} = u^4_{(\alpha,\beta)} & \text{on } \mathcal{S}^0, \quad \text{(40c)} \\ \varepsilon^3_{33} = \left(\widetilde{u}^F_3 - \widetilde{u}^{\chi_3}_3 \frac{M^F_3}{D_3} \right) F_{,3} - \left(\widetilde{u}^{V_\beta}_3 p_\beta + \frac{\widetilde{u}^{\chi_3}_3}{D_3} \left(\mu_3 - y^S_\beta \epsilon_{\beta\gamma} p_\gamma \right) \right) F \\ \qquad + U^3_{3,3} + y_\alpha U^2_{\alpha,33} & \text{on } \mathcal{S}^0, \quad \text{(40d)} \\ \sigma^3_{\alpha\beta} n_\beta = 0 & \text{on } \partial\mathcal{S}^0. \quad \text{(40e)} \end{cases}$$

The solution of this boundary value problem parametrized by the load F, its first gradient $F_{,3}$, the elongation $U^3_{3,3}$ and the curvatures $U^2_{\alpha,33}$. It writes as:

$$u^4_\alpha = \widetilde{u}^F_\alpha F + \widetilde{u}^{F\nabla}_\alpha F_{,3} + \widetilde{u}^{e_3}_\alpha U^3_{3,3} + \widetilde{u}^{\chi_\beta}_\alpha U^2_{\beta,33} + U^4_\alpha + y_\beta \epsilon_{\beta\alpha} \Theta^4, \tag{41}$$

The cross-section displacement $\widetilde{u}^F_\alpha$ is related to the non-uniform distribution in the section of the applied load $\widetilde{f}_\alpha$. Similarly, $\widetilde{u}^{F\nabla}_\alpha$ is related to the variations of F and the non-uniform distribution of $\widetilde{f_3}$ in the section.

Higher orders The induction process may be pursued any higher order. This leads to the derivation of new displacement localizations only related to higher derivatives of F relevant for faster variations of F.

Note that, the use of the asymptotic expansion method is based on the scaling in Equation (3). Hence the rescaled coordinates y_i have been used in the expression of the auxiliary problems $\mathcal{T}^p$ and $\mathcal{W}^p$. However, the distinction between the two sets of coordinates is no longer necessary in practice once the section modes are defined. The use of the coordinates y_i is therefore dropped in the following and replaced by the use of the coordinates x_i.

2.2 The higher-order beam model

Families of kinematic enrichment In the asymptotic expansion procedure, three families of kinematic enrichment emerged. First, the rigid motion of the section was carried by the six macroscopic variables U_i^p, $U_{\alpha,3}^p$ and Θ_3^p. They are respectively related to the following displacement modes:

$$\widetilde{\underline{\boldsymbol{u}}}^{U_1} = \begin{pmatrix} 1 \\ 0 \\ 0 \end{pmatrix}, \quad \widetilde{\underline{\boldsymbol{u}}}^{U_2} = \begin{pmatrix} 0 \\ 1 \\ 0 \end{pmatrix}, \quad \widetilde{\underline{\boldsymbol{u}}}^{U_3} = \begin{pmatrix} 0 \\ 0 \\ 1 \end{pmatrix}, \quad \widetilde{\underline{\boldsymbol{u}}}^{\Theta_2} = \begin{pmatrix} 0 \\ 0 \\ -x_1 \end{pmatrix}, \quad \widetilde{\underline{\boldsymbol{u}}}^{\Theta_1} = \begin{pmatrix} 0 \\ 0 \\ x_2 \end{pmatrix}, \quad \widetilde{\underline{\boldsymbol{u}}}^{\Theta_3} = \begin{pmatrix} -x_2 \\ x_1 \\ 0 \end{pmatrix}. \tag{42}$$

Second, the six correctors related to the six beam resultants[4] were derived: $\widetilde{u}_\alpha^{e_3}$, $\widetilde{u}_\alpha^{\chi_1}$, $\widetilde{u}_\alpha^{\chi_2}$, $\widetilde{u}_3^{\chi_3}$, $\widetilde{u}_3^{V_1}$, $\widetilde{u}_3^{V_2}$. They are also referred to as Saint Venant's modes [15, 12]. This collection of 12 modes (rigid and Saint-Venant) is denoted $\mathbb{B}^{\mathrm{SV}}$. Third, a family of modes related to the body force and its longitudinal variations was obtained: $\widetilde{\underline{\boldsymbol{u}}}^F, \widetilde{\underline{\boldsymbol{u}}}^{F\nabla}, \widetilde{\underline{\boldsymbol{u}}}^{F\nabla^2}$..., which is denoted $\mathbb{B}^f$. This suggests gathering all these modes in the following kinematic approximation for the 3D displacement:

$$\underline{\boldsymbol{u}} = \sum_{k=1}^{n} \widetilde{\underline{\boldsymbol{u}}}^k(x_\alpha) X^k(x_3) \tag{43}$$

where n is the number of modes and $X^k(x_3)$ are longitudinal unknown fields. It is demonstrated in [19] that the modes generated for a single prescribed body load distribution f_i in the cross-section is a Hilbert basis of the solution space for $\underline{\boldsymbol{u}}$.

Load superposition With proper scaling, it is possible to consider other loadings in a separate form between longitudinal coordinate and cross-section coordinates such as surface traction on the lateral boundary of the cross-section as well as prescribed eigenstrains. Furthermore, whereas most loadings in engineering practice comply with the separate form requested in equation (6) the latter may be too constraining in some specific cases. The problem being linear, it is possible to superpose loads. In that case, the collection of modes $\widetilde{\underline{\boldsymbol{u}}}^i$ may become linearly dependent and is orthogonalized.

In practice, it appears that decomposing a cross-section load distribution into several distinct loadings improves the quality of the solution. For instance, in Equation (6), one may modulate $\widetilde{f_3}(x_\eta)$ with $F(x_3)$ separately from $\widetilde{f_\alpha}(x_\eta)$ with another function $G(x_3)$. However, this doubles the number of kinematic degrees of freedom related to the applied load (third family). The best trade off between the load decomposition and the accuracy of the solution has not yet been explored in details.

[4] From the traction, bending and torsion constitutive equations (30) and (31), $\widetilde{u}_\alpha^{e_3}$, $\widetilde{u}_\alpha^{\chi_\beta}$ and $\widetilde{u}_3^{\chi_3}$ are directly related to N_3, M_β and M_3.

Minimum potential energy principle The higher-order beam model is obtained, inserting the approximated kinematics (43) in the minimum potential energy principle of the 3D problem (2). Indeed, the variable separation between longitudinal and cross-section coordinates allows the separation of the corresponding integrals. Since all cross-section modes are known there remains only a boundary value problem related to the longitudinal coordinate. The corresponding equilibrium equations write as:

$$\forall l, \quad X^k A_{kl} + X^k_{,3} \left(B_{kl} - B_{lk}\right) - X^k_{,33} C_{kl} - F_l = 0 \tag{44}$$

where:

$$\begin{aligned} &A_{kl} = \left\langle \widetilde{u}^k_{i,\alpha} C_{i\alpha j\beta} \widetilde{u}^l_{j,\beta} \right\rangle, \quad B_{kl} = \left\langle \widetilde{u}^k_i C_{i3j\beta} \widetilde{u}^l_{j,\beta} \right\rangle, \\ &C_{kl} = \left\langle \widetilde{u}^k_i C_{i3j3} \widetilde{u}^l_j \right\rangle, \quad \text{and} \quad F_k = \left\langle \widetilde{u}^k_i \widetilde{f}_i \right\rangle. \end{aligned} \tag{45}$$

Boundary conditions In the 3D problem (2), the beam extremities were assumed fully clamped. Considering the approximated kinematics (43), this is achieved enforcing $X_i = 0$ at extremities. Other boundary conditions may be applied. Indeed, the first six modes corresponds to the rigid motion of the section. Restraining only these degrees of freedom is actually the boundary condition classically used in structural mechanics: warping and transverse displacements are let free.

2.3 Applications

Two case study are briefly presented. The first case study illustrates the advantage of introducing displacement modes related to the distribution in the cross-section of the applied load. The second case study was extended to eigenstrains and illustrates the possibility of describing more accurately the effect of prestress in a beam. In both cases, the auxiliary problems (10) and (13) generating the kinematic enrichment were solved with 2D quadratic Lagrange finite elements. Two different strategies were used for the higher-order beam solution.

2.3.1 Cantilever box girder beam under a concentrated load

A cantilever beam of span 10 m with a box section 3 m wide is investigated (Figure 4). The width and the height of the box are 1 m. The thickness of the walls is 5 cm. The beam is fully clamped at its first extremity and loaded by a concentrated force in the middle of the section at the other extremity (Figure 4).

In addition to the six rigid modes (42) and the six Saint Venant modes ($\mathbb{B}^{\mathrm{SV}}$), 3 warping and 3 transverse displacement modes (Figure 5) are included in the kinematics ($\mathbb{B}^f$). These modes clearly illustrate the local influence of the distribution in the section of the concentrated load.

Because they lead to ordinary differential equations, beam models are suited for closed-form solutions. The homogeneous part of equations (44) have solutions of the form e^{kx_3} which may be found explicitly solving a quadratic eigenvalue problem [28]. This technique was used in [13] in order to find the solution of the beam loaded at its extremity. It presents the advantage to yield a solution extremely rapidly. However, because it may include sharp decaying exponential functions, its implementation requires specific treatment. Furthermore, it is restricted to linear problems with specific longitudinal distribution of the applied load. Figure 4 shows the reconstructed beam solution. The local settlement related to the application of the concentrated force is very well captured.

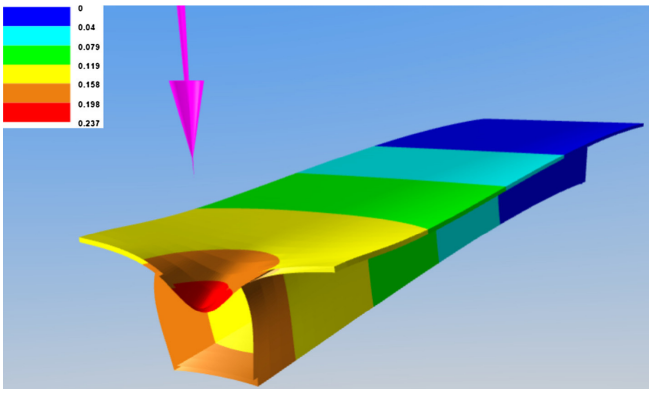

Fig. 4: Cantilever box girder beam under applied load [13]

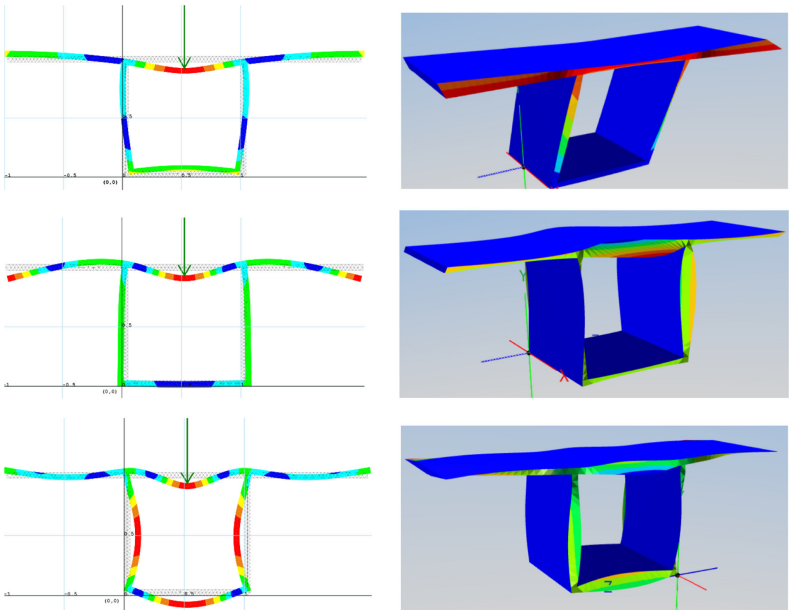

Fig. 5: Six displacement modes related to the applied load. Transverse modes (left) and warping modes (right). [13]

2.3.2 *Prestressed cable in a cantilever beam*

The higher-order beam model is further illustrated with a cantilever concrete beam prestressed with a steel cable. The section of the beam is represented in Figure 6. The beam is 20 m long. The concrete domain is denoted by Ω_c and the steel domain by Ω_s. A constant eigenstrain $\boldsymbol{\varepsilon}^* = \varepsilon^*_{33}\underline{\boldsymbol{e}}_3 \otimes \underline{\boldsymbol{e}}_3$ is applied in Ω_s, with $\varepsilon^*_{33} = 7.10^{-3}$, corresponding to 23 MN pretension in the cable. Both materials are homogeneous and isotropic with: $(E, \nu)_{\text{concrete}} = (35\text{ GPa}, 0.2)$ and $(E, \nu)_{\text{steel}} = (200\text{ GPa}, 0.3)$. Note that, a real concrete beam would require additional reinforcement bars as well as a non-linear constitutive behavior. This simplified example is

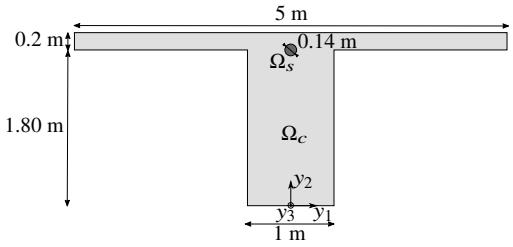

Fig. 6: Section of the prestressed beam

chosen here to illustrate the ability of eigenstrain modes to capture rather fast variations of the strain in the section.

The sectional modes are computed up to the fourth gradient of the eigenstrain. The 5 first orthonormalized modes associated to the eigenstrain $\widetilde{\underline{\boldsymbol{u}}}^{T}$, $\widetilde{\underline{\boldsymbol{u}}}^{\nabla T}$, $\widetilde{\underline{\boldsymbol{u}}}^{\nabla T^2}$, $\widetilde{\underline{\boldsymbol{u}}}^{\nabla T^3}$ and $\widetilde{\underline{\boldsymbol{u}}}^{\nabla T^4}$, denoted $\mathbb{B}^{\varepsilon}$, are represented in Figure 7. These three transverse modes and two warping modes clearly illustrate the action of the cable in the concrete beam.

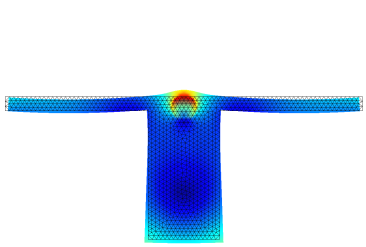

(a) Transverse mode $\underline{\boldsymbol{u}}^{T}$

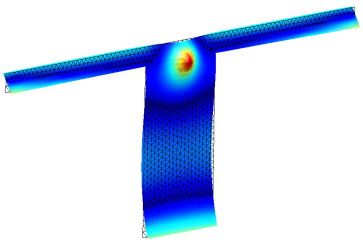

(b) warping mode $\underline{\boldsymbol{u}}^{\nabla T}$

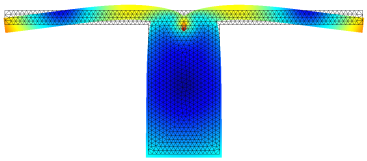

(c) Transverse mode $\underline{\boldsymbol{u}}^{\nabla T^2}$

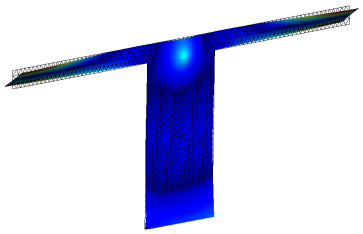

(d) warping mode $\underline{\boldsymbol{u}}^{\nabla T^3}$

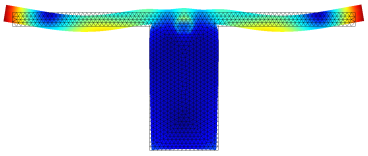

(e) Transverse mode $\underline{\boldsymbol{u}}^{\nabla T^4}$

Fig. 7: The 5 eigenstrain modes related to the prestress in the steel cable used in case study 2.

	reference model	**higher-order beam model**
type of elements	15-nodes pentahedron	6-nodes triangle + 41 longitudinal knots
number of elements	99680	1788 + 1
CPU computation time	1805 s	24 s

Table 1: Main features of the 3D solution and solution S

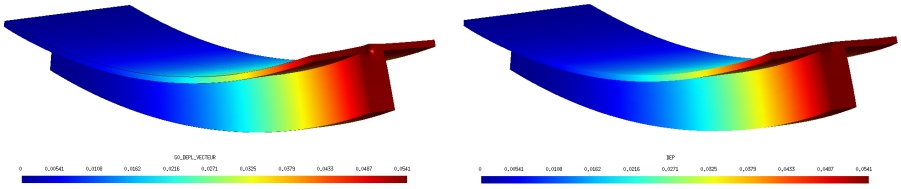

(a) 3D computation (b) Higher-order beam model

Fig. 8: Deformed structure under pre-tensioned steel cable (amplification factor = 100), [9]

The higher-order beam model was discretized with NURBS shape functions. Contrary to the closed-form solution previously mentioned, this allows to apply various load distributions. Additionally, NURBS shape functions are known to mitigate locking phenomena. This was confirmed in a detailed study of the present implementation in [9].

The reconstructed solution is presented in Figure 8. As expected, the prestressed cable compresses and raises the beam. The higher-order beam model captures transverse displacements illustrated by the lowering of the edges of the table. It also captures warping displacements illustrated by the punching effect of the cable which can be observed at the end of the beam. A 3D reference solution was also computed by means of *Code_Aster* on a very similar mesh. The deformed beam is also presented in Figure 8 and the computation data is summarized in Table 1. It appears that, the model presented here shows very satisfying results with a significantly reduced computational cost. Indeed, only very few additional modes (3 to 5) and their corresponding beam DOF were required for capturing fairly well the applied eigenstrain. These time performances can still largely be improved by more advanced implementations and numerical techniques.

However, detailed analysis shows that in the vicinity of the boundaries, the quality of the solution is not as satisfying as in the bulk of the beam (see details in [9]). This is not surprising since higher-order convergence results has only been obtained in configurations were boundary layers related to the beam extremities are not present. In order to better describe the mechanical behavior close to boundary conditions, the approach developed independently by *Strains Engineering* consists in the introduction of new modes specific to these boundary conditions in the reduced basis.

3 The Asymptotic Expansion Load Decomposition elasto-plastic beam model

Introducing elasto-plastic behavior is more challenging. The inherent non-linearity of plasticity and the incremental nature of plastic analysis makes the definition of a relevant kinematics more difficult. Two main approaches are followed when solving an elasto-plastic

beam problem: 1D elasto-plastic beam model based on a priori cross-section analysis or 3D elasto-plastic beam models based on a 3D beam kinematics.

The first natural approach is to express the plastic flow in terms of generalized beam variables and to solve an elasto-plastic 1D problem. This requires the elasto-plastic analysis of the cross-section for pure or combined generalized stresses and the derivation of the corresponding yield surface. The cross-section analysis may be incremental or based on limit analysis but assumes a uniform distribution of generalized stresses in the longitudinal direction: normal force, shear forces, bending moments and torque. A key difficulty is the derivation of a yield surface directly function of the beam generalized stress taking into account correctly their possible interactions as well as hardening. There were recent improvements in this direction, approximating the yield surface with facets or ellipsoids [5]. Once the yield surface is defined, there remains to compute the elasto-plastic response of the beam, either with closed form solutions [25], limit analysis [22] or by means of finite element approximations [3, 23]. This approach has the advantage to present fast computation time, since only a 1D elasto-plastic problem needs to be solved. However, its accuracy remains limited by the beam theory assumptions. First, it cannot handle local phenomena related to the distribution of the applied load as well as to the boundary conditions. Second, it provides only an averaged description of the actual stress in the beam.

In order to improve the accuracy of the beam model, the second classical approach consists in setting a beam kinematics expressing the 3D displacement field in a separate form between the transverse coordinates and the longitudinal coordinate. This kinematics may be defined a priori or may evolve during the incremental procedure. For a fixed increment of the generalized displacements, the corresponding 3D stress is computed and the yield criterion is expressed locally. A local algorithm such as the radial return is processed on the whole body to compute the local plastic state of the beam. This locally admissible stress state is integrated on each cross-section yielding the corresponding longitudinal distribution of the beam generalized stresses. Finally, the beam global equilibrium is ensured with a standard Newton-Raphson procedure. The main difficulty lies again in the definition of a relevant kinematics able to describe the displacement related to plastic flow.

Most approaches where the kinematics is fixed a priori rely on the ones already discussed in linear elasticity such as Euler-Bernoulli, Timoshenko kinematics or even Saint-Venant solution, eventually with non-linear geometric corrections. Once the kinematics is defined, there remains to choose the number of integration points in the cross-section in order to compute precisely the local plastic flow. Multiplying integration points improves the accuracy of the results at the price of a higher computation time of the cross-sections integrals. This is the spirit of multi-fiber beam models (see for instance [18]). Another direction is to enrich arbitrarily the section kinematics with degrees of freedom not necessarily related to classical cross-section displacements. This concept was formalized extensively by Carrera et al [7] and co-workers.

Because plastic flow may not be easily known *a priori* a natural improvement of the preceding methods is to update the beam kinematics during the load increments. This is the direction followed here using the asymptotic expansion.

3.1 Adaptation of the higher-order beam model to the elasto-plastic behavior

The linear higher-order beam model presented in the previous section is extended to elasto-plasticity in the small strains framework. Hence, the boundary value problem expressed in

Equation (2) is now considered with a J_2 elasto-plastic constitutive law and will be solved classically following a Newton-Raphson incremental scheme.

As for linear elasticity, a 3D approximated kinematics is formulated in a separated form in order to perform the dimension reduction. The first collection of modes to take into account is the basis of Saint Venant modes $\mathbb{B}^{\text{SV}}$ as well as the basis of force modes $\mathbb{B}^{f}$ related to the applied load described previously. Nevertheless, this kinematics is not sufficient for describing accurately the possibly discontinuous plastic flow which may occur in the cross section. Therefore, the plastic strain computed at a given iteration of the Newton-Raphson procedure is taken into account for enriching the kinematics of the following iteration. This is possible using the procedure described in the previous section for a fixed plastic strain $\boldsymbol{\varepsilon}^{\text{p}}$ distribution in the cross-section. Considering now the whole beam, $\boldsymbol{\varepsilon}^{\text{p}}$ is not longitudinally uniform. Hence, several chosen cross-sections may be used for taking snapshots of the plastic strain in order to sufficiently enrich the kinematics of the model. These new *plastic modes* are computed and added to the kinematics on the fly. The basis of modes specific to a cross-section plastic strain distribution is denoted by $\mathbb{B}^{\varepsilon}$. Finally, the kinematics of the model is evolving during the Newton-Raphson procedure and is the union of the basis $\mathbb{B}^{\text{SV}}$, $\mathbb{B}^{f}$ and $\mathbb{B}^{\varepsilon}$. This union of basis is orthonormalized to form the total basis $\mathbb{B}$ with a total number of modes n_{mod}.

This approach presents two major advantages. First, it does not require additional elasto-plastic computations in the cross-section. Second, the number of beam degrees of freedom remains very limited (about 20) thanks to the sparsity of the kinematics. From the optimality result proved in [19], this approach is expected to be more efficient than arbitrary kinematic refinements.

Note that, contrary to Nonuniform Transformation Field Analysis [20, 21, 14] where a basis of plastic strains is introduced with the corresponding plastic multipliers, in the present approach, *displacement* plastic modes are added to the *total* 3D displacement approximation and plasticity is processed at each integration point of the 3D body.

3.2 The elasto-plastic algorithm

The implementation of the general framework introduced in the previous section is now detailed. This requires first the definition of the numerical approximation of the 3D body. Then, the incremental resolution of the elasto-plastic problem is adapted so that processing the local constitutive equations remains standard whereas the global equilibrium iterations are performed with the reduced basis.

3.2.1 Numerical approximation of the higher-order beam model

The approach suggested in the previous section requires the definition of a 3D mesh of the beam composed of cross-sections meshes positioned along the longitudinal direction (Figure 9). Indeed, these cross-sections will be the domain of integration of the constitutive law.

Longitudinal discretization A longitudinal discretization of the beam is defined for the generalized displacements $X^m(x_3)$ introduced in Equation (43). The same collection of NURBS basis functions for each $X^m(x_3)$ is chosen:

$$X^m(x_3) = \sum_{i=1}^{n_{\text{NURBS}}} N^i(x_3) X^{m,i} \tag{46}$$

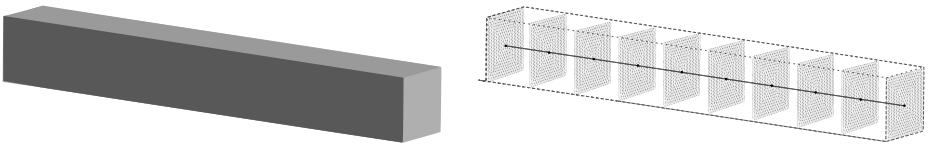

Fig. 9: Discretization of a square beam

where $N^i(x_3)$ are the NURBS interpolation function and $X^{m,i}$ are the corresponding degrees of freedom. A set of $N_s > n_{\text{NURBS}}$ longitudinal integration points is also defined for the integration of the interpolation functions. It is natural to place the cross-section meshes at the positions of these longitudinal integration points.

Cross-section discretization The cross-section mesh used for the computation of the modes is the same as the one used in Section 2.3.2: the modes are computed by means of quadratic Lagrange triangle elements:

$$\tilde{\underline{\boldsymbol{u}}}^m(x_\alpha) = \sum_{j=1}^{n_{\text{sec}}} \underline{\boldsymbol{L}}^j(x_\alpha)\widetilde{u}^{m,j} \tag{47}$$

where n_{sec} is the number of nodes in the section, $\underline{\boldsymbol{L}}^j(x_\alpha)$ are Lagrange interpolation functions and $\widetilde{u}^{m,j}$ are the nodal values of the displacement.

The local state variables, $\Delta\boldsymbol{\varepsilon}$, $\Delta\boldsymbol{\varepsilon}^{\text{p}}$ and $\Delta\boldsymbol{\sigma}$ are computed in the N_s cross-sections meshes at the Gauss points of the quadratic triangle elements.

Plastic-mode cross-section During the computation, sections where a plastic strain is not zero are collected. All cross-sections where plasticity occurs could be used for the computation of the plastic modes: for each plastic strain distribution in each cross section, one or several modes could be computed. However, it would excessively increase the number of generalized displacement degrees of freedom n_{dof} and also increase the computation time dedicated to the corresponding modes. In order to limit the number of plastic modes to a few, only one cross-section called *plastic-mode cross-section* is chosen for taking snapshots of the plastic strain distribution. As a first approach, this choice is based on an educated guess.

3.2.2 Adaptation of the Newton-Raphson procedure

Formulation of the tangent stiffness of the beam model For a given basis of n_{mod} displacement modes, the numerical approximation of the total displacement may be written as follows:

$$\underline{\boldsymbol{u}}(\underline{\boldsymbol{x}}) = \sum_{m=1}^{n_{\text{mod}}} \sum_{i=1}^{n_{\text{NURBS}}} \sum_{j=1}^{n_{\text{sec}}} \underline{\boldsymbol{L}}^j(x_\alpha) N^i(x_3)\, \widetilde{u}^{m,j} X^{m,i} = \sum_{i=1}^{n_{\text{NURBS}}} \sum_{j=1}^{n_{\text{sec}}} \underline{\boldsymbol{L}}^j(x_\alpha) N^i(x_3) u^{i,j} \tag{48}$$

where the $n_{\text{3D}} = n_{\text{NURBS}} \times n_{\text{sec}}$ local displacement degrees of freedom are:

$$u^{i,j} = \sum_{m=1}^{n_{\text{mod}}} \widetilde{u}^{m,j} X^{m,i}. \tag{49}$$

Considering the second form of (48), it appears that the 3D strain $\varepsilon(\underline{\boldsymbol{u}})$ and consequently the local constitutive equation may be directly computed from $u^{i,j}$ without the need to specify

the basis $\mathbb{B}$. Hence, provided the finite element solution is stored as the collection of the $u^{i,j}$, the local integration of the constitutive equations as well as the computation of the local elasto-plastic tangent stiffness remain unchanged compared to a 3D formulation.

For a fixed basis $\mathbb{B}$, injecting the numerical approximation of the kinematics (48) into the principle of virtual work corresponding the elasto-plastic 3D problem (2) leads to the expression of the residual expressed in terms of the increment of the $n_{\text{dof}} = n_{\text{mod}} \times n_{\text{NURBS}}$ generalized displacement degrees of freedom $\Delta X^{m,i}$ and the corresponding test degrees of freedom. The standard Newton-Raphson procedure is used in order to cancel this residual which leads to the following formal reduced equilibrium equation:

$$[\boldsymbol{K}^{\text{ep}}]_{\mathbb{B}} \left\{\delta \underline{\boldsymbol{X}}\right\}_{\mathbb{B}} = \{\boldsymbol{R}\}_{\mathbb{B}} \,, \tag{50}$$

where $[\boldsymbol{K}^{\text{ep}}]_{\mathbb{B}} \in (\mathbb{R}^{n_{\text{dof}}})^2$ is the global tangent stiffness matrix of the beam model expressed in basis $\mathbb{B}$, computed with the local elasto-plastic tangent stiffness, $\left\{\delta \underline{\boldsymbol{X}}\right\}_{\mathbb{B}}$ is the finite element vector of the generalized degrees of freedom $\delta X^{m,i}$ and $\{\boldsymbol{R}\}_{\mathbb{B}} \in \mathbb{R}^{n_{\text{dof}}}$ is the residual vector. Because, the tangent stiffness as well as the residual both depend on the choice of the basis $\mathbb{B}$, they need to be updated each time the basis is changed.

Significant computational time is gained because n_{dof} which sets the size of the tangent stiffness is much smaller than the rather large $n_{3\text{D}}$ which is required for a sufficiently detailed description of the fields in the cross-section.

Description of the numerical procedure The basis of modes $\mathbb{B}$ is first initialized and is composed $\mathbb{B}^{\text{SV}}$ and n_{fAE} modes associated to the applied load $\mathbb{B}^{f}$. While increments do not generate plastic flow, the basis $\mathbb{B}$ remains unchanged. The global tangent stiffness corresponds to the elastic one and each increment is solved in one iteration.

Let assume that increment n generates a non-vanishing plastic strain $\Delta\boldsymbol{\varepsilon}_n^{\text{p}}$ at the first iteration $k = 1$. In this case, before starting the second iteration, the basis of modes is enriched and orthonormalized with n_{pAE} modes computed from the plastic strain distribution $\Delta\boldsymbol{\varepsilon}_n^{\text{p}}$ observed in the plastic-mode cross-section, following [9]. This also requires the update of the residual.

It has been noticed from experience that plastic modes computed at subsequent iterations of the increment were very similar. Therefore the basis $\mathbb{B}$ used at iteration $k = 2$ is kept until the convergence of the increment is reached. However, the converged plastic strain of the increment $\Delta\boldsymbol{\varepsilon}_n^{\text{p}}$ may have changed. Hence, at the first iteration $k = 1$ of the following increment $n + 1$, the basis $\mathbb{B}$ is updated, replacing only plastic modes with new ones. Again, at the second iteration $k = 2$ the basis is updated and then remains fixed until the convergence of the increment. This choice of updating the plastic modes only at the first two iterations of the increment remains valid as long as the load increments are not too important.

3.3 Application to a cantilever beam

To illustrate the efficiency of the model presented, a steel beam clamped at one end and loaded on its free end is investigated. The beam is a wide flange beam HE600M. This cross-section is class 1 in Eurocode 3, meaning that the beam reaches its limit of elasticity with no risk of local buckling. The geometry of the 6 m long beam is detailed in Figure 10. A load is applied with eccentricity at the top edge of the free end of the beam, as represented in Figures 10 and 11. The force F is applied on the length $l = 230$ mm. The study is decomposed into 10 time steps, and the load is incrementally increased of 0.25 MN at each step until it reaches

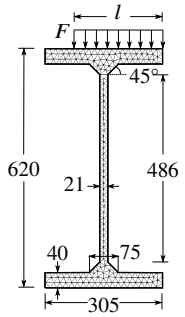

Fig. 10: Dimensions (mm) of the HE600M section, mesh and applied load

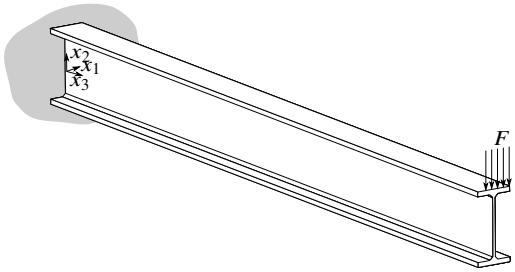

Fig. 11: 3D representation of the HE600M cantilever beam loaded at its end

2.5 MN and then it is released following the reversed path. The following values are chosen for the Young's modulus the Poisson's ratio, the strain hardening modulus and the yield modulus:

$$E = 210\ \text{GPa}, \qquad \nu = 0.3, \qquad H = 0.02E, \qquad \sigma_0 = 235\ \text{MPa} \tag{51}$$

Higher-order beam solution S_{1D} The section of the solution S_{1D} is meshed with 399 quadratic triangle Lagrange elements, as shown in Figure 10. The NURBS interpolation functions are represented in Figure 12. The corresponding integration sections are represented in Figure 13. The mesh is refined close to the clamped extremity since plasticity is expected to occur mainly at this location.

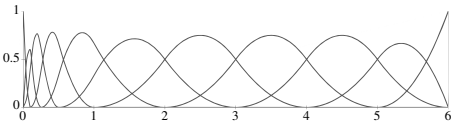

Fig. 12: Second-order NURBS basis functions used for the longitudinal interpolation of the element

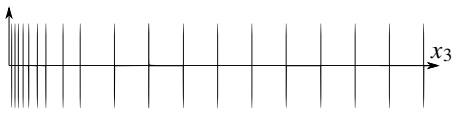

Fig. 13: Longitudinal mesh composed of 19 integration sections

The plastic-strain cross-section is placed at $x_3 = 0.25$ m at the 5^{th} integration point. The number of force modes is $n_{\text{fAE}} = 4$, and of plastic modes is $n_{\text{pAE}} = 9$. During the computation, the maximum number of modes in the basis is 22. Indeed, in the orthormalization procedure, redundant modes are discarded. The number of interpolation shape functions being 11, the maximum number of degrees of freedom during the computation is therefore $n_{\text{dof}} = 242$.

3D Reference solution A 3D reference solution is computed with the finite element software *Code_Aster*. The beam is meshed by extruding a cross-section with 430 triangles along the longitudinal axis. The longitudinal discretization is the same as for the beam model and forms 7740 prismatic elements in total. The prismatic elements are interpolated with quadratic functions.

Comparison with the 3D reference solution The beam solution is 80 times faster to compute. The corresponding deformed structure is presented in Figure 14. The torque due to the eccentricity of the load induces a longitudinal rotation of the cross-section, and the transverse part of the load induces a bending of the beam.

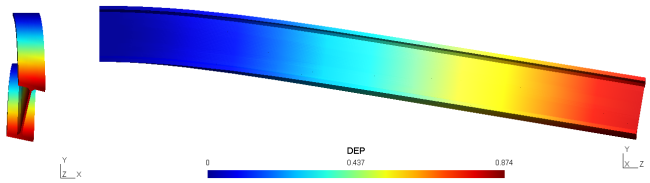

Fig. 14: Deformed shape of the beam after the 10 load increments (solution S_{1D})

In order to compare both solutions, the deflection at point A placed on the free extremity of the beam ($x_3 = 6$ m) is represented in Figure 15 during the 20 time steps of the study. The

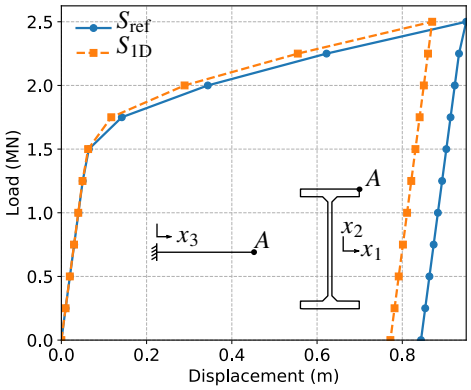

Fig. 15: Deflection at point A for loading and unloading

results obtained with the beam solution S_{1D} are consistent with the reference solution. The beam solution satisfactorily captures the plastic branch despite a low kinematic hardening ($H = 0.02E$). The curve of S_{1D} is slightly above the curve of S_{ref}: for $u_A = 0.8$ m, solution S_{1D} associates a force $2,42\%$ higher than the force obtained by S_{ref}. As expected, the unloading occurring between time steps t_{11} and t_{20} is elastic. The gap between the beam solution and the 3D solution induces a difference between the two residual displacements observed at t_{20}. For the solution S_{1D} considered here, the relative distance between the two solutions at t_{20} is of 8.51%. This relative distance originates from the gap observed at t_{10} which is maintained between t_{11} and t_{20} since the unloading is elastic. A residual displacement closer to the 3D reference could be obtained with more refined longitudinal meshes and with higher interpolation order for the interpolation functions. But in regards with the very low computational time offered by the beam solution, the results obtained can be considered satisfying for engineering applications.

In order to assess the accuracy of the beam solution when compared to the reference solution the six components of the plastic strain computed by the solution S_{1D} and by the reference solution at $x_3 = 0,5$ m for the given displacement $u_A = 0.8$ m of point A, are presented in Figure 16. All the variables presented for a fixed displacement of point A are obtained by linear interpolations between the increments defined in Section 3.3 and figured by markers in Figure 15.

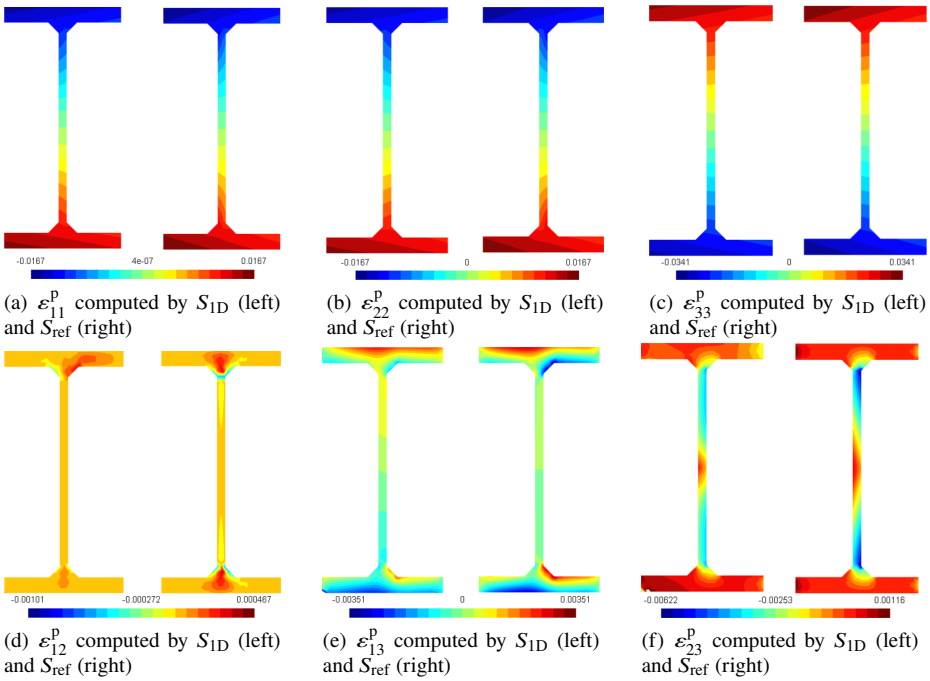

(a) $\varepsilon^{\mathrm{p}}_{11}$ computed by S_{1D} (left) and S_{ref} (right)

(b) $\varepsilon^{\mathrm{p}}_{22}$ computed by S_{1D} (left) and S_{ref} (right)

(c) $\varepsilon^{\mathrm{p}}_{33}$ computed by S_{1D} (left) and S_{ref} (right)

(d) $\varepsilon^{\mathrm{p}}_{12}$ computed by S_{1D} (left) and S_{ref} (right)

(e) $\varepsilon^{\mathrm{p}}_{13}$ computed by S_{1D} (left) and S_{ref} (right)

(f) $\varepsilon^{\mathrm{p}}_{23}$ computed by S_{1D} (left) and S_{ref} (right)

Fig. 16: Plastic strain in solutions S_{1D} and S_{ref} close to the clamped extremity at $x_3 = 0.5$ m for $u_A = 0.8$ m

The axial plastic strain presented in Figures 16a to 16c shows that nearly all parts of the section have reached the elastic limit. As expected, the eccentricity of the load on the free extremity of the beam creates a slightly uneven progression of plasticity in the section. Therefore the highest values of the plastic strain components are observed at the top left and the bottom left of the section where the absolute values of the stresses are largest. The plastic strain computed by S_{1D} is slightly lower than the plastic strain computed by S_{ref} for each component. A late detection of plasticity due to the longitudinal refinement is suspected to originate this phenomenon.

The non-axial components presented in Figures 16d to 16f seem less satisfying but their amplitude is about 10 times lower than the axial components. Thus, the beam solution presented here shows satisfying results with a good comparison with the 3D solution.

4 Discussion and outlooks

Several applications of the AELD higher-order elasto-plastic beam model were presented. The model is based on an enrichment of the reduced kinematics updated on the fly and does not need any *a priori* knowledge on the solution of the problem.

Both in linear elasticity framework and in J_2 elastoplasticity, the beam model required a computation about 80 times shorter than for the reference 3D solution computed on *Code_Aster* with comparable meshes. These gains in computation time are already very interesting and could be even larger by means of parallelization, in particular for the computation of the tangent stiffness matrix.

The numerical differences between the beam solution and the reference solution for the examples presented are low, and could still be lowered. Indeed, the computation of the displacement modes is optimal only far from boundary conditions. At the clamped extremity the local stress varies rapidly. The model could therefore be improved if displacement modes specific to the boundary conditions were computed and added to the kinematics of the model. Furthermore, the choice of the plastic-mode cross-section was arbitrary and could be automated based for instance on the location of the first occurence of plasticity in the beam.

We conclude that the present beam model offers already interesting perspectives for engineering applications on the cloud. Nevertheless, it is meant to be validated on more complex case-studies.

Several extensions of the linear elastic AELD model are straightforward. The low and medium frequency dynamic behavior is easy to derive including inertia contributions from the assumed kinematics [26]. Buckling analysis may also be adapted [27], as the eigenstrains enrichment is a suitable basis for representing the pre-stress in the beam and deriving the geometric stiffness operator. Similarly, other weak couplings (thermal, humidity, creep etc.) or non standard physics [17] may be incorporated in the model. . Furthermore, the elasto-plastic beam model has been presented here with an isotropic material and a J_2 yield criterion. Its adaption to different yield criteria is easy and the extension to more complex materials like reinforced concrete was achieved with a Rankine yield criterion in [11].

Finally, as long as strains remains small, the kinematic enrichment provided by the asymptotic expansion remains relevant. Hence, the authors are considering a co-rotational formulation of the AELD beam model in order to introduce geometric non-linearities related to large displacements and rotations.

References

1. Actis RL, Szabo BA, Schwab C (1999) Hierarchic models for laminated plates and shells. Computer Methods in Applied Mechanics and Engineering 172(1-4):79–107, DOI 10.1016/S0045-7825(98)00226-6, URL http://linkinghub.elsevier.com/retrieve/pii/S0045782598002266
2. Amrouche C, Ciarlet PG, Gratie L, Kesavan S (2006) On the characterizations of matrix fields as linearized strain tensor fields. Journal de Mathématiques Pures et Appliquées 86(2):116–132, DOI 10.1016/j.matpur.2006.04.004, URL http://linkinghub.elsevier.com/retrieve/pii/S0021782406000535
3. Argyris JH, Boni B, Hindenlang U, Kleiber M (1982) Finite element analysis of two- and three-dimensional elasto-plastic frames-the natural approach. Computer Methods in Applied Mechanics and Engineering 35(2):221–248, DOI 10.1016/0045-7825(82)90135-9

4. Benscoter S (1954) A theory of torsion bending for multi-cell beams. URL http://www.scopus.com/inward/record.url?eid=2-s2.0-0003341622&partnerID=tZOtx3y1
5. Bleyer J, de Buhan P (2013) Yield surface approximation for lower and upper bound yield design of 3D composite frame structures. Computers and Structures 129:86–98, DOI http://dx.doi.org/10.1016/j.compstruc.2013.08.011, URL http://www.sciencedirect.com/science/article/pii/S0045794913002411
6. Buannic N, Cartraud P (2001) Higher-order effective modeling of periodic heterogeneous beams. I. Asymptotic expansion method. International Journal of Solids and Structures 38(40-41):7139–7161, DOI 10.1016/S0020-7683(00)00422-4, URL http://www.sciencedirect.com/science/article/B6VJS-43TP9JM-7/2/f294534047362a0262c1cafbdbf47fed http://linkinghub.elsevier.com/retrieve/pii/S0020768300004224
7. Carrera E, Giunta G, Petrolo M (2011) Beam Structures. John Wiley \& Sons, Ltd, Chichester, UK, DOI 10.1002/9781119978565, URL http://doi.wiley.com/10.1002/9781119978565
8. Ciarlet PG, Ciarlet P (2004) Another approach to linearized elasticity and Korn's inequality. Comptes Rendus Mathematique 339(4):307–312, DOI 10.1016/j.crma.2004.06.021, URL http://linkinghub.elsevier.com/retrieve/pii/S1631073X0400322X
9. Corre G, Lebée A, Sab K, Ferradi MK, Cespedes X (2018) Higher-order beam model with eigenstrains: theory and illustrations. ZAMM - Journal of Applied Mathematics and Mechanics / Zeitschrift für Angewandte Mathematik und Mechanik 98(7):1040–1065, DOI 10.1002/zamm.201700180, URL http://doi.wiley.com/10.1002/zamm.201700180
10. Corre G, Lebée A, Sab K, Ferradi MK, Cespedes X (2018) The Asymptotic Expansion Load Decomposition elastoplastic beam model. International Journal for Numerical Methods in Engineering DOI 10.1002/nme.5926, URL http://doi.wiley.com/10.1002/nme.5926
11. Corre G, Lebée A, Sab K, Ferradi MK, Cespedes X (2019) A new higher-order elastoplastic beam model for reinforced concrete. Meccanica DOI 10.1007/s11012-019-01003-5, URL http://link.springer.com/10.1007/s11012-019-01003-5
12. El Fatmi R (2016) A refined 1D beam theory built on 3D Saint-Venant's solution to compute homogeneous and composite beams. Journal of Mechanics of Materials and Structures 11(4):345–378, DOI 10.2140/jomms.2016.11.345, URL http://msp.org/jomms/2016/11-4/p02.xhtml
13. Ferradi MK, Lebée A, Fliscounakis A, Cespedes X, Sab K (2016) A model reduction technique for beam analysis with the asymptotic expansion method. Computers & Structures 172:11–28, DOI 10.1016/j.compstruc.2016.05.013, URL http://linkinghub.elsevier.com/retrieve/pii/S0045794916302656
14. Fritzen F, Leuschner M (2013) Reduced basis hybrid computational homogenization based on a mixed incremental formulation. Computer Methods in Applied Mechanics and Engineering 260:143–154, DOI 10.1016/j.cma.2013.03.007, URL http://linkinghub.elsevier.com/retrieve/pii/S0045782513000583
15. Iesan D (1976) Saint-Venant's problem for inhomogeneous and anisotropic elastic bodies. Journal of Elasticity 6(3):277–294, DOI 10.1007/BF00041722, URL http://link.springer.com/10.1007/BF00041722
16. Jouravskii DI (1856) Remarques sur la résistance d'un corps prismatique et d'une pièce composée en bois ou en tôle de fer à une force perpendiculaire à leur longueur. Annales des Ponts et Chaussées 12:328–351, URL http://gallica.bnf.fr/ark:/12148/bpt6k4084868/f331.item

17. Lurie S, Solyaev Y (2019) On the formulation of elastic and electroelastic gradient beam theories. Continuum Mechanics and Thermodynamics 31(6):1601–1613, DOI 10.1007/s00161-019-00781-3, URL https://doi.org/10.1007/s00161-019-00781-3
18. Mazars J, Kotronis P, Ragueneau F, Casaux G (2006) Using multifiber beams to account for shear and torsion. Applications to concrete structural elements. Computer Methods in Applied Mechanics and Engineering 195(52):7264–7281, DOI 10.1016/j.cma.2005.05.053
19. Miara B, Trabucho L (1992) A Galerkin spectral approximation in linearized beam theory. Mathematical Modelling and Numerical Analysis 26(3):425–446
20. Michel J, Suquet P (2003) Nonuniform transformation field analysis. International Journal of Solids and Structures 40(25):6937–6955, DOI 10.1016/S0020-7683(03)00346-9, URL http://linkinghub.elsevier.com/retrieve/pii/S0020768303003469
21. Michel J, Suquet P (2004) Computational analysis of nonlinear composite structures using the nonuniform transformation field analysis. Computer Methods in Applied Mechanics and Engineering 193(48):5477–5502, DOI http://dx.doi.org/10.1016/j.cma.2003.12.071, URL http://www.sciencedirect.com/science/article/pii/S004578250400283X
22. Olsen PC (1999) Rigid plastic analysis of plane frame structures. Methods 179:19–30
23. Papadrakakis M, Papadopoulos V (1995) A computationally efficient method for the limit elasto plastic analysis of space frames. Computational Mechanics 16(2):132–141, DOI 10.1007/BF00365867
24. Sanchez-Palencia E (1980) Non-Homogeneous Media and Vibration Theory, Lecture Notes in Physics, vol 127. Springer Berlin Heidelberg, Berlin, Heidelberg, DOI 10.1007/3-540-10000-8, URL http://adsabs.harvard.edu/abs/1980LNP...127.....S http://www.springerlink.com/index/10.1007/3-540-10000-8 http://link.springer.com/10.1007/3-540-10000-8
25. Štok B, Halilovič M (2009) Analytical solutions in elasto-plastic bending of beams with rectangular cross section. Applied Mathematical Modelling 33(3):1749–1760, DOI 10.1016/j.apm.2008.03.011, URL http://linkinghub.elsevier.com/retrieve/pii/S0307904X08000826
26. Taig G, Ranzi G, D'Annibale F (2015) An unconstrained dynamic approach for the Generalised Beam Theory. Continuum Mechanics and Thermodynamics 27(4-5):879–904, DOI 10.1007/s00161-014-0358-5
27. Taig G, Ranzi G, Luongo A (2016) GBT pre-buckling and buckling analyses of thin-walled members under axial and transverse loads. Continuum Mechanics and Thermodynamics 28(1-2):41–66, DOI 10.1007/s00161-014-0399-9
28. Tisseur F, Meerbergen K (2001) The Quadratic Eigenvalue Problem. SIAM Review 43(2):235–286, DOI 10.1137/S0036144500381988, URL http://epubs.siam.org/doi/abs/10.1137/S0036144500381988 http://epubs.siam.org/doi/10.1137/S0036144500381988
29. Trabucho L, Viaño J (1996) Mathematical modelling of rods, vol 4. Elsevier Science B. V., DOI 10.1016/S1570-8659(96)80006-8, URL http://www.sciencedirect.com/science/article/pii/S1570865996800068 http://linkinghub.elsevier.com/retrieve/pii/S1570865996800068
30. Vogelius M, Babuška I (1981) On a Dimensional Reduction Method I. The Optimal Selection of Basis Functions. Mathematics of Computation 37(155):31, DOI 10.2307/2007498, URL http://www.jstor.org/stable/2007498?origin=crossref
31. Vogelius M, Babuška I (1981) On a Dimensional Reduction Method II. Some Approximation-Theoretic Results. Mathematics of Computation 37(155):47, DOI

669 10.2307/2007499, URL http://www.jstor.org/stable/2007499?origin=crossref
670 32. Zhao Q, Cartraud P, Kotronis P (2015) Justification of the asymptotic expansion
671 method for homogeneous isotropic beams by comparison with the Saint-Venant so-
672 lution. Journal of Elasticity 126(2):245–270, DOI 10.1007/s10659-016-9593-2, URL
673 http://dx.doi.org/10.1007/s10659-016-9593-2 http://link.springer.com/10.1007/s10659-
674 016-9593-2